

Signal modulation and processing in nonlinear fibre channels by employing the Riemann-Hilbert problem

Morteza Kamalian, Anastasiia Vasylchenkova, Dmitry Shepelsky, Jaroslaw E. Prilepsky,
and Sergei K. Turitsyn, *Fellow, OSA*

Abstract—Most of the nonlinear Fourier transform (NFT) based optical communication systems studied so far deal with the burst mode operation that substantially reduce achievable spectral efficiency. The burst mode requirement emerges due to the very nature of the commonly used version of the NFT processing method: it can process only rapidly decaying signals, requires zero-padding guard intervals for processing of dispersion-induced channel memory, and does not allow one to control the time-domain occupation well. Some of the limitations and drawbacks imposed by this approach can be rectified by the recently-introduced more mathematically-demanding periodic NFT processing tools. However, the studies incorporating the signals with cyclic prefix extension into the NFT transmission framework have so far lacked the efficient digital signal processing (DSP) method of synthesising an optical signal, the shortcoming that diminishes the approach flexibility. In this work we introduce the Riemann-Hilbert problem (RHP) based DSP method as a flexible and expandable tool that would allow one to utilise the periodic NFT spectrum for transmission purposes without former restrictions. First, we outline the theoretical framework and clarify the implementation underlying the proposed new DSP method. Then we present the results of numerical modelling quantifying the performance of long-haul RHP-based transmission with the account of optical noise, demonstrating the good performance quality and potential of RHP-based optical communication systems.

Index Terms—Fibre-optic communications, nonlinear Fourier transform, nonlinear inverse synthesis, periodic nonlinear Fourier transform.

I. INTRODUCTION

Historically, the classical communication theory was developed for linear channels. However, it is well known that the fibre-optic channels are essentially nonlinear due to the Kerr effect: modulation, transmission, detection and processing techniques optimal for nonlinear fibre channels are yet to be revealed. One of such truly nonlinear approaches (coined eigenvalue communications) was proposed in [1]: it is based on the special properties of the master model [2] that approximately describes nonlinear fibre channels in certain limits. The concept of eigenvalue communication was resurrected and largely extended recently under the

M. Kamalian, A. Vasylchenkova, J. E. Prilepsky and S. K. Turitsyn are with the Aston Institute of Photonic Technologies, Aston University, Birmingham, B4 7ET, UK. D. Shepelsky is with B.Verkin Institute for Low Temperature Physics and Engineering, 47 Nauky Ave., Kharkiv, 61103, Ukraine and V.N.Karazin Kharkiv National University, 4 Svobody Square, Kharkiv, 61022, Ukraine.

e-mail: kamali@aston.ac.uk (M. Kamalian)

name of NFT-based transmission, see, e.g., recent papers [3, 4] and references therein. The anticipated advantage of NFT-based optical communication systems is their potential “nonlinearity-immune” performance, and the NFT processing has been shown to be a promising technique for the mitigation of nonlinear fibre distortion with various system designs studied in recent years [4–12, 20].

It should be mentioned that NFT is just another name (frequently used in engineering community) for the inverse scattering transform method invented for the solution of a specific class of nonlinear equations – the so-called integrable equations [2, 13]. A lot of research has been done in this field by the mathematical community and future engineering work can take advantage of these previous mathematical studies. As was shown in the seminal work by Zakharov and Shabat [2], the nonlinear Schrödinger equation (NLSE) belongs to the aforementioned class of integrable equations and have many remarkable properties that allow one to describe signal evolution in such nonlinear systems by applying the NFT. Simultaneously, the NLSE is the key model governing in certain limits and under specific conditions signal propagation in single-mode optical fibres [4, 14]. In this work we will focus only on the NLSE-based communication channels, though these ideas can be expanded to more general cases. The central idea behind the NFT-based communication system is to use, in order to carry the encoded data, the so-called nonlinear (NFT) spectrum of a signal [1]. The advantage of such an approach is that the NFT spectrum evolution in an idealised (described by lossless and noiseless NLSE) nonlinear optical fibre is linear, and the spectral “bands” defined within the NFT domain are free from the nonlinear cross-talk [3, 4]. This is in contrast to the “conventional” information transmission in coherent optical systems, where the nonlinear cross-talk that is widely considered to be one of the factors limiting conventional systems performance [14, 15].

Insofar, most of the studies related to the NFT-based communication systems have dealt with the signal processing using NFT methods developed in formal mathematical terms for an infinite time interval [2, 4]. In such a situation, signal under consideration, formally defined on the infinite extent, has to decay in time sufficiently fast (has to have a finite L_1 norm [13], to be more mathematically specific). Of course, in real-world applications, the truncated waveforms are used. When the “insufficient portion” of the signal is

processed, or when the neighbouring NFT symbols overlap due to a weak time-decay rate or dispersive spreading, the noticeable performance penalty emerges [16, 17]. Even with such limited NFT approach, there have already been a number of experimental confirmations that the NFT-based techniques do indeed have the potential for mitigation of nonlinear penalties [8–10, 18–20].

However, despite the promising performance of the systems based on the “conventional NFT”, they all still have drawbacks and limitations coming from the current type of commonly used NFT processing. Aside from some technical problems related to the utilisation of “unusual” NFT-generated pulses (the systems’ sensitivity to transceiver imperfections [4, 7] and optical noise [17]), and the issues related to the NFT routines performance as the signal power and/or processing interval grow [3, Part II], [6, 16, 21, 22], which are rather just the peculiarities of the method, we mention more fundamental issues: (i) the hardly-controllable (and typically extended) optical signal duration after the inverse NFT at the transmitter [7, 20, 23]; (ii) a large processing window required, involving the full dispersion-induced memory; (iii) high signal power fluctuation in a stream of transmitted symbols [4]. The latter means that compared to the current version of NFT-based schemes where the dispersion-induced memory either the same or exceeds the information-bearing batch duration, the periodic NFT systems render a much lower PAPR (peak-to-average power ratio) level. (The difficulties when INFT is applied to long-duration pulses were underlined in [21, 22])

In this respect, considering the *periodically-continued* signals and respective NFT processing type (periodic NFT, PNFT) one can relax or even eliminate some of the aforementioned problems [24]. In particular, the period of PNFT-generated signal and, hence, the symbol duration are well controllable parameters. Note that this problem can also be dealt with by means of recently-introduced “*b*-modulation” NFT-based method [56, 57]. The power fluctuation of periodically-continued signals is much lower due to the absence of zero-padding “wings” in-between the information-bearing time intervals (symbols), and for the current NFT methods, where the dispersion memory is comparable with the signal duration, the PNFT renders a significant reduction in PAPR. Within the PNFT we have to process just one (predefined) period reducing the processing window and, hence, the number of samples to process [24, 26], and the overall complexity of a DSP processing [25]. The latter basically comes from the advantage of using cyclic extension in PNFT. Using periodic solutions, one can introduce cyclic extension instead of the zero guard intervals between data batches. As the signal propagates through the fibre, it broadens due to the chromatic dispersion. As far as the length of this guard band (cyclic extension) is greater than the channel memory, the signal broadening can be compensated. At the receiver, it is required for the whole broadened signal to be processed. This means that some information of the signal slips out of the original time window, T , into the extended wings of length $\mu/2$, where $\mu/2$ is equal to the channel memory, see Eq. (10).

However, due to the presence of the cyclic extension, the original time duration of the signal, T , contains all the information necessary to recover data and there is no need to process the rather large window of size $T + \mu$. This fact can also result in the performance improvement due to ISI reduction, as the spreading of the neighbouring symbols affect the central part less than the “wings”.

The signal-to-noise ratio (SNR) degradation due to signal-noise interference, proportional to the processing interval duration for the transmission inside the NFT domain [17, 27], can be diminished due to the shorter processing window as well. A PNFT-based system can have, in addition, a better overall spectral efficiency due to the smaller time-bandwidth product of the signal [28]. Another benefit of PNFT, as will be explained later, is the lower computational complexity of the inverse transformation numerical routines in comparing with the available conventional NFT ones. In our approach of constructing a periodic signal by solving a RHP, the RHP is solved for each point in time, hence, the complexity scales linearly with the number of time samples of the signal which is to be compared to the best available algorithm with $O(N \log^2 N)$ proposed in [58]. This also helps parallelise the computation in our proposed approach which. Thus, the PNFT applied to optical transmission allows us to retain the “conventional” NFT advantages, but can render a lot of beneficial features itemised above. The challenge is a growing mathematical complexity behind PNFT-based methods.

Within the PNFT-based communication concept, we have to deal with the periodic solutions of nonlinear integrable equations. The latter have been the subject of study for a long time [29–33], and their vast application area ranging from water gravity waves to optical turbulence, has encouraged researchers to develop a solid mathematical base for their description [34–36]. In particular, there exists the analogue of inverse scattering method (the NFT, in other words) for periodic “boundary conditions” [24, 35–40]. Finding the nonlinear spectrum of a periodic function (the direct PNFT) at the receiver (Rx) side can be done using the fast PNFT algorithm described in Ref. [41]: the complexity here is close to that of the fast Fourier transform. We also mention some earlier numerical PNFT methods with improved complexity [35].

The main challenge in PNFT-based communication arises from the inverse transformation at the transmitter (Tx) side: constructing a periodic signal in time domain given the modulated nonlinear (PNFT) spectrum components (nonlinear modes). To the best of our knowledge, there is still a lack of a generic and effective method to perform the inverse PNFT, and more active involvement of mathematicians would be greatly beneficial here. There exist approaches suitable for particular nonlinear solutions and respective PNFT spectra types [42]. However, these methods have a somewhat limited flexibility compared to quite versatile conventional NFT-transmission approaches [4, 7]. The same problem holds when the periodic solutions with simple known PNFT spectra are used [26, 28, 43–45], which can be understood as the analogue of eigenvalue

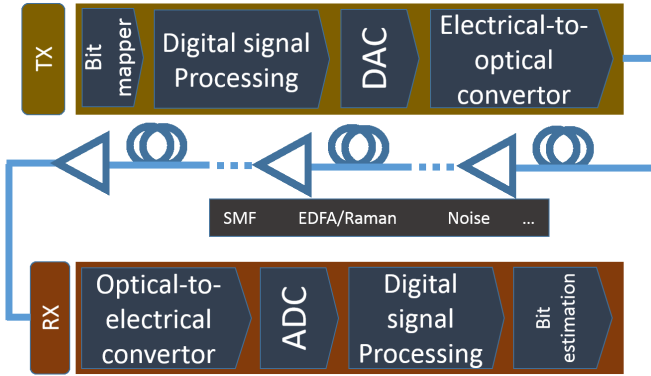


Fig. 1: The schematic of a communications system with the DSP processing modules at Tx and Rx. In particular, for our research the DSP at Tx side includes the RHP solution, while at the Rx side the processing described at Appendix B is used.

communication idea [1], the progenitor of NFT-based techniques. The main technical challenges in the computation of inverse PNFT at the Tx side are related to the accurate Riemann theta function computation and Jacobi inversion problem, see Ref. [24] and referenced therein for more details.

In this paper we propose and develop the new DSP method for the PNFT-based transmission (Fig. 1) that allows one to compute the inverse PNFT harnessing the numerical solution of RHP [47] attributed to the NLSE [48]. In this work, as a proof-of-concept, we design a relatively simple communication system based on the RHP signal processing at the Tx side considering the so-called finite-genus solutions of NLSE. The finite-genus solutions are generally quasi-periodic, but the periodicity can be ensured by imposing some additional constraints on the PNFT spectrum, see [42] and also Eq. (27) and the mentioned argument about it.

The paper is organised as follows. In Sec. II we briefly describe the conventional approach for the computation of finite-genus solutions, which employs their algebro-geometric description on Riemann surfaces, and then we itemise the difficulties that arise comparing it with the RHP method. In Sec. III we present the RHP approach for constructing periodic finite-genus solutions of the NLSE. These results are then used in Sec. IV to illustrate the procedure of data mapping onto the nonlinear spectrum and to design a communication system. Further we elucidate how one can manipulate system's parameters and compute the communication-related characteristics of the signal. Simulation results are given in Sec. V. The elements of Floquet theory used for direct PNFT are given in Appendix A, and the RHP formalism for constructing the finite-genus solutions is outlined in Appendix B. In Appendix C we discuss the transformation of the RHP in view of improving effectiveness of its numeric implementation. In this work bold symbols mean vectors and matrices (e.g. \mathbf{I} denotes a

2×2 identity matrix), with the exception of Pauli matrices,

$$\sigma_2 = \begin{pmatrix} 0 & -i \\ i & 0 \end{pmatrix} \quad \text{and} \quad \sigma_3 = \begin{pmatrix} 1 & 0 \\ 0 & -1 \end{pmatrix}.$$

The complex unity in this study is denoted as i , \Re and \Im are the real and imaginary parts of a complex number, correspondingly, and asterisk means complex conjugate.

II. MATHEMATICAL BACKGROUND: THE ALGEBRO-GEOMETRIC APPROACH FOR THE COMPUTATION OF INVERSE PNFT

A. Basic properties of nonlinear spectrum in periodic NFT

Finite-genus (also called finite-gap) NLSE solutions arise when the spectrum of the associated linear operator (2), defined below, consists of a finite number of arcs. Here we write down the NLSE in the dimensionless form (see Ref. [4] for the explanation of normalisations),

$$iq_z + q_{tt} + 2|q|^2 q = 0, \quad (1)$$

where q is the normalised light-envelope function, t is the retarded time, and z is the normalised distance along the fibre. Eq. (1) here is explicitly written for the most interesting case of anomalous dispersion. It is the celebrated Zakharov-Shabat system of auxiliary linear equations, which has the same form for any NFT type (periodic or infinite-duration) attributed to NLSE:

$$\Phi_t = \begin{bmatrix} -i\lambda & q(t, z) \\ -q(t, z)^* & i\lambda \end{bmatrix} \Phi, \quad (2)$$

considered on the whole line $t \in \mathbb{R}$, where $q(t, z)$ is a solution to NLSE (1), $\Phi(t, z, \lambda)$ is a two-element (vector) eigenfunction, and λ is the spectral parameter that can be thought of as a nonlinear analogue of frequency. If the “potential” in (2) is periodic, i.e., $q(t, z) = q(t+T, z)$ for some period T , then the spectrum of (2) consists of finite or infinite number of arcs (see Fig 2a) symmetric w.r.t. \mathbb{R} . The so-called *main spectrum* consists of the end points of the spectral arcs (some details are given in Appendix A; for more information, see [37, 39]). If the number of arcs is finite, the “potential” is called finite gap or finite-genus; the latter term comes from its construction involving objects defined on a Riemann surface of finite genus, see Section II-B below. In this case, the main spectrum consists of pairs of complex conjugated numbers, $\{\lambda_j, \lambda_j^*\}$, $j = 0, 1, \dots, \mathcal{N}$ for a genus- \mathcal{N} solution. If $q(t, z)$ satisfies the NLSE (1), the spectral arcs (and thus their end points λ_j) are independent of z (similar to the soliton eigenvalues of “conventional” NFT [2, 4, 13]). These arcs constitute the continuous nonlinear spectrum part locus, in contrast to the “conventional” NFT, where the continuous spectrum locus is the real axis, see Fig. 2.

B. Algebro-geometric approach

Finite-genus solutions of Eq. (1) are conventionally expressed in terms of meromorphic functions, differentials and integrals on hyperelliptic Riemann surfaces of finite genus, see [40]. The construction of such solutions (usually called in this context *algebro-geometric*) involves the following steps:

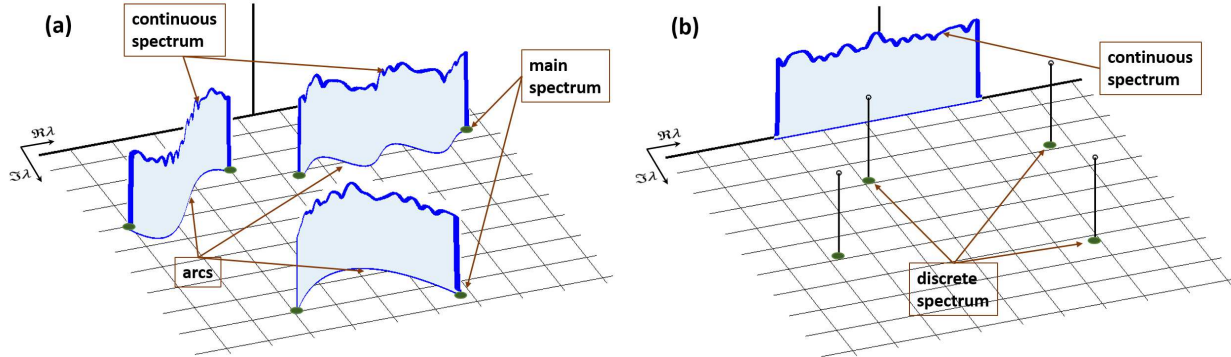


Fig. 2: a) Nonlinear spectrum of a periodic signal with multiple continuous spectra and the main spectrum as the endpoints of the arcs, and b) Nonlinear spectrum of a vanishing boundary signal with a continuous spectrum and the discrete spectrum as the singular complex points independent of the location of the continuous spectrum.

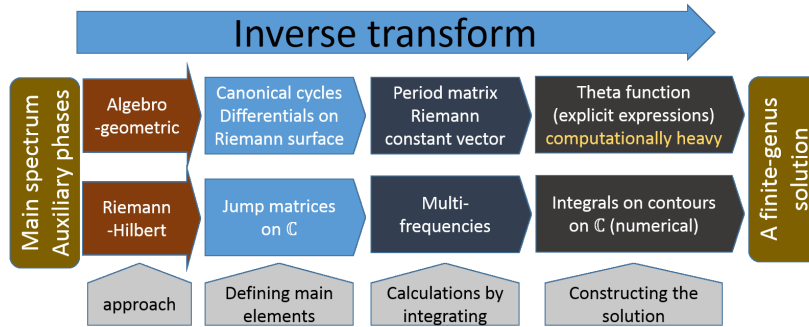


Fig. 3: The procedure of the inverse transformation with algebro-geometric approach (upper row) and solving a Riemann-Hilbert problem (lower row).

- (i) Given $\{\lambda_j\}$, $j = 0, 1, \dots, \mathcal{N}$, introduce the Riemann surface \mathcal{X} associated with the algebraic curve $F(w, \lambda) = 0$ having the form

$$w^2 = \prod_{j=0}^{\mathcal{N}} (\lambda - \lambda_j)(\lambda - \lambda_j^*).$$

Introduce the canonical basis of oriented circles (a_j, b_j) , $j = 1, \dots, \mathcal{N}$, on \mathcal{X} and define the associated objects: the period matrix B , the basis of holomorphic differentials ω , and the Abel integrals Ω_j , $j = 1, 2, 3$, fixed by their particular behaviour at ∞^\pm (the infinity points at two sheets of \mathcal{X}).

- (iii) Determine the scalar parameters E , N , and α from the asymptotic expansions of Ω_j at ∞^\pm , and the vector parameters \mathbf{V} , \mathbf{W} , and \mathbf{r} by $V_j = \int_{b_j} d\Omega_1$, $W_j = \int_{b_j} d\Omega_2$,
 $j = 1, \dots, \mathcal{N}$, $\mathbf{r} = \int_{\infty^-}^{\infty^+} \boldsymbol{\omega}$.

(iv) Given B , determine the Riemann theta function

$$\Theta(u_1, \dots, u_{\mathcal{N}}) = \sum_{\mathbf{l} \in \mathbb{Z}^{\mathcal{N}}} \exp \left[\frac{1}{2} (B \mathbf{l}, \mathbf{l}) + (\mathbf{l}, \mathbf{u}) \right], \quad (3)$$

where $(\mathbf{l}, \mathbf{u}) = l_1 u_1 + \dots + l_N u_N$.

- (iv) Given an additional \mathcal{N} -dimensional vector \mathbf{D} , determine the solution $q(t, z)$ of (1) by

$$q(t, z) = \alpha \frac{\Theta(i\mathbf{V}t + i\mathbf{W}z - \mathbf{D} + \mathbf{r})}{\Theta(i\mathbf{V}t + i\mathbf{W}z - \mathbf{D})} \frac{\Theta(\mathbf{D})}{\Theta(\mathbf{D} - \mathbf{r})} e^{-iEt + iNz}.$$

Although the construction of $q(t, z)$ above can be considered as explicit, its numerical implementation faces several drawbacks, one of them being related to the numerical calculation of Riemann theta function. The first step in the calculation of Θ as a multi-dimensional Fourier series is to truncate the grid from which the vectors \mathbf{l} are drawn, to a bounded subspace of \mathbb{C}^N , thus introducing the sampling of the frequency-wavenumber domain, $\mathbf{V} - \mathbf{W}$. This itself introduces some error in the calculations, which can be controlled to some extent by considering the contribution of different terms along the series [46]. However, if this bounded grid is limited to integers between $-M_1$ and M_1 , the number of terms in (3) is $(2M_1 + 1)^N$ which grows exponentially with the number of arcs. However, the argument of Riemann theta function in Eq. (3), contains literally linear dependency on time. Taking this into account, we can ensure the periodicity using a commensurable set of frequencies, C_j^f (see appendix B) to convert the multi-dimensional series into an ordinary Fourier series. In this way, calculating the Riemann theta function is turned into a Fourier series with time-dependent coefficients coming from another Fourier series [35]. Considering this approach, which is called the hyperfast method of evaluating the Riemann theta function [35], the complexity of constructing a periodic signal with N time samples is

$$O\left(N\mathcal{N}(2M_1+1)^{\mathcal{N}} \log(2M_1+1)\right)$$

Although the latter property helps decrease the computational complexity, it remains considerably heavy especially when compared to its alternative that is rendered by the RHP approach, see Sec. III.

III. CONSTRUCTING A PERIODIC FINITE-GAP SOLUTION VIA THE SOLUTION OF A RHP

The same NLSE solutions can be constructed in terms of the solutions of RHP [48], which is based on the auxiliary factorisation problem defined in the complex plane of spectral parameter λ entering Zakharov-Shabat system (2): given jump matrices on $\mathcal{N}+1$ arcs connecting λ_j with λ_j^* , find a (matrix-valued) function which is analytic outside the arcs, whose limiting values from the both sides of the arcs are related through the given jumps, and whose large- λ behaviour is prescribed (for details, see Appendix B). A remarkable features of this RHP is that the dependence of the jumps on the independent variables t and z of the NLSE solution appears in an explicit, exponential way. Particularly, this implies that no time or space stepping is required to obtain the value of the solution at a specific t and z . In turn, solving the RHP reduces to solving an integral equation for a function determined by the union of the arcs, for which an efficient numeric implementation is now available [49, 50] (more on the computational complexity follows). A schematic comparison between the stages of constructing a periodic solution for the NLSE using the algebro-geometric and RHP approaches is shown in Fig. 3. NLSE, being an integrable nonlinear equations, can be represented as the compatibility condition for a Lax pair of auxiliary linear equations, consisting of Zakharov-Shabat system (2), determining the nonlinear spectrum of a pulse at a given z , and the second equation, determining the evolution of the nonlinear spectral data [2]:

$$\Phi_z = \mathbf{R}(t, z, \lambda)\Phi, \quad (4)$$

where

$$\mathbf{R}(\lambda, t, z) = \begin{bmatrix} i|q|^2 - 2i\lambda^2 & 2\lambda q + iq_t \\ -2\lambda q^* + iq_t^* & -i|q|^2 - 2i\lambda^2 \end{bmatrix}. \quad (5)$$

The RHP associated with a genus- \mathcal{N} solution to the NLSE has a distinguished feature that its jump matrices are constants (w.r.t. λ) on each connected part of the jump contour: each individual arc of the contour is determined by the main spectrum $\{\lambda_j\}_{j=0}^{\mathcal{N}}$ whereas the jump matrix associated with this arc is determined by the real “phases” $\{\phi_j\}_{j=0}^{\mathcal{N}}$ (an analogue of vector D in the algebro-geometric approach), see (7) below. Associated with this data set $\{\{\lambda_j\}_{j=0}^{\mathcal{N}}, \{\phi_j\}_{j=0}^{\mathcal{N}}\}$ is the so-called (planar) Baker-Akhiezer function $\Phi(t, z, \lambda)$, which is a special solution of both Eqs. (2) and (4) that can be uniquely characterized by the following conditions:

- (i) For any t and z , $\Phi(t, z, \lambda)$ is analytic, 2×2 -valued function of λ in $\mathbb{C} \setminus \Gamma$ with $\Gamma = \cup_{j=0}^{\mathcal{N}} \Gamma_j$ and $\Gamma_j = (\lambda_j, \lambda_j^*)$ is the arc connecting λ_j and its complex conjugate.

- (ii) The limiting values Φ^\pm of Φ , as λ approaches both the sides of Γ_j , are related through the jump conditions:

$$\Phi^-(t, z, \lambda) = \Phi^+(t, z, \lambda) \mathbf{J}_j, \quad \text{for } \lambda \in \Gamma_j, \quad j = 0, \dots, \mathcal{N}, \quad (6)$$

$$\mathbf{J}_j = \begin{bmatrix} 0 & ie^{-i\phi_j} \\ ie^{i\phi_j} & 0 \end{bmatrix}. \quad (7)$$

- (iii) As $\lambda \rightarrow \infty$, the limiting value satisfies

$$\Phi(t, z, \lambda) = \left[\mathbf{I} + O(\lambda^{-1}) \right] e^{(-i\lambda t - 2i\lambda^2 z)\sigma_3}. \quad (8)$$

The associated genus- \mathcal{N} solution $q(t, z)$ of the NLSE is

$$q(t, z) = 2i(\Phi_1(t, z))_{1,2}$$

(where $(\cdot)_{1,2}$ denotes the $(1, 2)$ matrix entry), where $\Phi_1(t, z) = \lim_{\lambda \rightarrow \infty} \lambda (\Phi(t, z, \lambda) e^{(i\lambda t + 2i\lambda^2 z)\sigma_3} - \mathbf{I})$. To construct the time domain waveform given the set of parameters $\{\{\lambda_j\}_{j=0}^{\mathcal{N}}, \{\phi_j\}_{j=0}^{\mathcal{N}}\}$, we need to define the jump matrices, \mathbf{J}_j and solve a RHP to arrive at $\Phi(t, z, \lambda)$ and eventually $q(t, z)$. The most involved part in this scheme is to solve the RHP (more precisely, to solve a family of RHP parametrized by t and z). It can be reduced (and then implemented numerically) to solving an integral equation for a function determined on the union of all arcs, see Appendix B. We refer the reader to detailed book [47] for the numerical realisation of this step. For our purpose, in this work we will use the existing numerical package RHPackage [49]. Using RHSolve subroutine from RHPackage we note that in order to solve the RHP we need to deal with fast discrete cosine transform (DCT) and compute Cauchy integral (21) at n Chebyshev points of the second kind, where n is the total number of spectral points on the arcs (directly related to the resolution $\Delta\lambda$ between the adjacent discretisation points). The numerical error is shown to decay spectrally as n grows [50], see also Appendix D. Computing (21) can be significantly expedited by expanding the solution using the Chebyshev polynomials of the first kind inasmuch as the expressions for the Cauchy integral involving these polynomials are known explicitly. Evaluating the n Chebyshev polynomials can be done using $O(n \log n)$ floating point operations. To facilitate comparison between the complexity of evaluating the Riemann theta function with solving the RHP, keeping the spectral resolution, $\Delta\lambda$ fixed (i.e. $n = n_0 \mathcal{N}$ where n_0 is the number of points over each cut), one can find the computational complexity of our proposed method to be

$$O(N \mathcal{N} n_0 \log(\mathcal{N} n_0) + NM(\mathcal{N} n_0)),$$

where $M(n_1)$ is the complexity of solving an $n_1 \times n_1$ linear system. The equation above shows that as opposed to evaluating the Riemann theta, the computational complexity of solving the RHP does not scale exponentially with the number of cuts which is going to be important when the approach is generalised to a higher symbol per signal communication. This feature is the principle advantage with respect to the alternative approach of the construction of algebro-geometric solutions where the Riemann theta functions (3) are used, see Subsec. II-B. It is worth noting

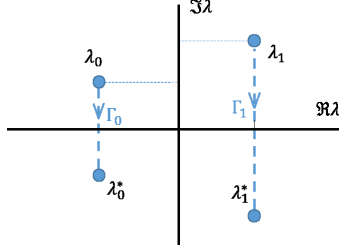


Fig. 4: Exemplary main spectrum of a genus-1 signal: which shows complex λ -plane with the cuts Γ_j along the arcs (λ_j, λ_j^*) , and endpoints $\{\lambda_j, \lambda_j^*\}$. In our study the data are mapped on the imaginary parts of eigenvalues.

that the number of cuts can have indirect influence on the accuracy of the numerical routines through the requirements of the application. For example, if increasing the genus entails a larger bandwidth which in turn enhances the fibre distortion, the system will need more accurate numerical calculations realised by more time samples. Another note is that, there are periodic solutions to the NLSE with analytically known closed form based on the algebro-geometric approach that can provide two real degrees of freedom while avoiding the Riemann theta function [42, 51, 52]. However, these signals are not generalisable to a more symbol per signal case while our RHP approach is. Notice also that the RHP approach guarantees (by the requirement that all ϕ_j 's in (7) are real) that the solution satisfies the focusing NLSE (and not just a NLS system). This is an advantage over the algebro-geometric approaches for nonlinear equations associated with non-self-adjoint Lax spectral problems (like the focusing NLSE), where the loci of the auxiliary spectrum points are not prescribed beforehand, and thus a special care should be taken (as is done, for example, in [51] in the genus-1 case only) in order to determine physically relevant classes of solutions (this problem is called the “reality problem” [40]).

IV. A COMMUNICATION SYSTEM BASED ON PERIODIC NFT

To have a signal capable of carrying one complex QAM symbol in its PNFT (main) spectrum, we use a genus-1 solution as the most straightforward non-trivial case. The exemplary main spectrum is shown in Fig. 4. For simplicity, we also do not make use of the additional PNFT parameters $\phi_{0,1}$ from (7) for our building up the simple proof-of-concept communication system here, setting $\phi_0 = \phi_1 = 0$.

A. Data mapping, optical signal construction, and its parameters evaluation

As it was indicated in Sec. III, for our simple genus-1 system we can ensure the periodicity of the underlying $q(t, z)$ in t by applying an appropriate shift along the real axis to the whole spectral picture in Fig. 4, see eq. (27) and remarks in the paragraph below it. On the other hand, the difference between the real parts of λ_0 and λ_1 is related to the value of the period. Thus, if we want to have

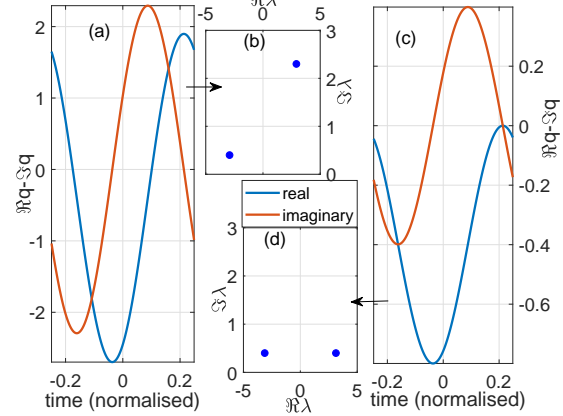


Fig. 5: Examples of a signal waveform, panes (a) and (c), constructed from the main spectra shown in panes (b) and (d), respectively (only the region $\Im \lambda > 0$ is depicted).

some predefined period, we can adjust the real parts of λ_0 and λ_1 , and the QAM symbol can be constructed by modulating their imaginary parts. In other words, knowing the imaginary part of the eigenvalues and a given signal period, T (and thus fixing $C^f = 2\pi/T$, see (28)), we can find the real parts of λ_0 and λ_1 . The coefficient C^g in eq. (28) is then calculated, the jump matrices from (29) are defined, and the solution of the RHP (30) is obtained using the RHPackage for WOLFRAM MATHEMATICA [49]. Two example signals obtained in such a way (together with their main spectrum) are shown in Fig. 5 via a procedure illustrated in Fig. 6. Now notice that the real parts of λ_0 and λ_1 are associated with the signal bandwidth: when we keep the imaginary parts fixed, the larger the distance between the real parts, the greater the bandwidth. The signal period $T = 2\pi/C^f$ is also affected by this distance; being rather a complicated function of this distance in general, it turns to be an almost linear function of it in the range applicable for practical purpose, see Fig. 7a. The signal bandwidth dependency is shown in Fig. 7b. For our simulations we choose to have a signal with bandwidth of around $\Delta v = 5$ GHz. These calibration plots allow us to choose a proper value for the difference in real parts to guarantee the desirable signal period. On the other hand, the signal power (or energy, to be more accurate) depends on the imaginary parts of the points of the main spectrum: the larger the imaginary parts, the higher the power. For small difference of the real parts, the signal power is determined by the largest imaginary part (panes (a) and (b) in Fig. 8), and thus we can fix the largest imaginary parts and manipulate with the second one, keeping the power value almost unchanged. For a larger difference, both points of the main spectrum are equally involved in defining the signal power value (see panes (c) and (d) in Fig. 8). Due to the perturbing noise (numerical, receiver and amplifier noise), the signal power has a lower bound below which it is impossible to discern the information bearing eigenvalues from the noise-induced spurious ones. We have found this lower limit by performing some simulations

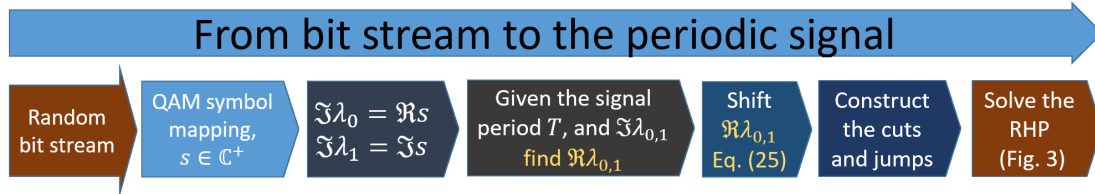


Fig. 6: The procedure of modulating the NS from a random bit stream.

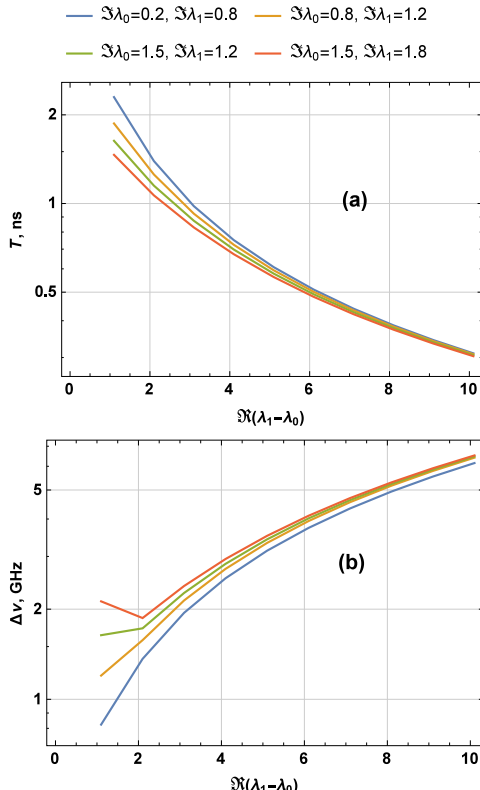


Fig. 7: Dependencies of (a) the signal period, and (b) the bandwidth on difference between the real parts of eigenvalues, for various combinations of imaginary parts..

and have chosen a value large enough to minimise the possibility of spurious eigenvalue being mistaken for a data-bearing one. On the other hand, the upper bound on the signal power is determined by the numerical errors in nonlinear signal processing and more pronounced signal-noise interaction. Therefore, the imaginary parts of the eigenvalues can be seen as $\Im\lambda_{0,1} = I_0 + (l-1)\Delta I, l = 1, \dots, \sqrt{M}$ where I_0 is the smallest imaginary part imposed by noise, ΔI is the step size, and M is the constellation size. In the case considered in our work, a QAM constellation, made up by the imaginary parts of two main spectrum points, contains a point corresponding to a signal with the lowest power (the left bottom point of the constellation, see Fig. 9 for example) and other points corresponding to higher signal powers (having larger $\Im\lambda_{0,1}$). Increasing the signal power by raising the imaginary part of the main spectrum points makes the distance between the constellation points

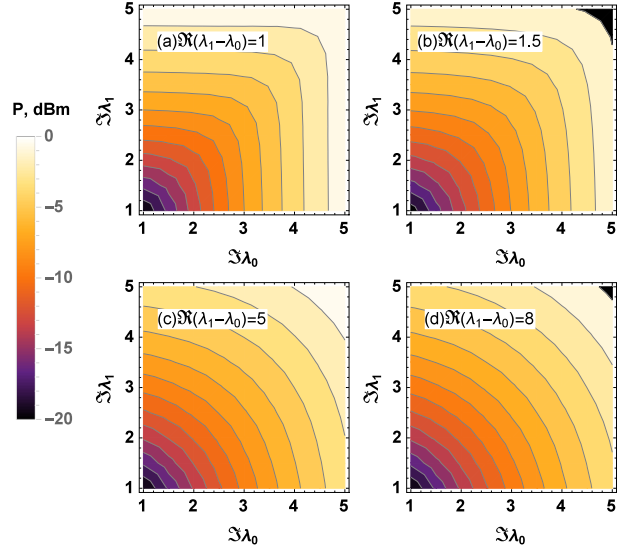


Fig. 8: The power of the genus-1 solution as function of the imaginary parts of the main spectrum for various differences between the real parts.

grow farther. Thus, the probability of the constellation points crossing the decision boundaries at the receiver gets lower. The consequence of controlling the signal power by means of changing the imaginary part of the eigenvalues (changing the SNR) and the ability to control the error by scaling the constellation are the main reason why we have chosen the imaginary parts of the spectrum points to carry the data. The real parts are determined by the desired signal period and the chosen imaginary parts. However, we note that the effective SNR defined inside the PNFT domain is an involved function of the signal power and distance between the constellation points: we can not have a better performance by simply enlarging the constellation size. So the interrelation between the system performance and signal power (constellation size) is studied through numerical simulations in the following section.

V. SIMULATION RESULTS

In this section, simulation results for a system with signal (22) in a fibre link with ideal Raman amplification and in a link with lumped amplification (using EDFA) are presented. The block diagram of the communication system is depicted in Fig. 1. The fibre characteristics chosen are those of a standard single mode fibre: $\alpha = 0.2$ dB/km, $\beta_2 = -20$ ps²/km and $\gamma = 1.3$ /W/km, and the span length of

80 km is considered. For the links with Raman amplification and EDFA the noise power spectral density, N_{ASE}^R and N_{ASE}^E respectively, are given by the expressions [14]:

$$N_{ASE}^R = \alpha L h v_s K_T, \quad N_{ASE}^E = (e^{\alpha L} - 1) h v_s n_{sp}, \quad (9)$$

where $h v_s$ is the photon energy, $n_{sp} \approx 1$ and $K_T \approx 1.13$ are the amplification parameters. In the simulations, when the lumped amplification (with EDFA) is used, it is necessary to adopt a path-average model for the fibre link to take into account the impact of periodic loss and amplification in the framework of NFT (PNFT). Using such a model, we apply the adjustment explained in [45] to optimise the location of amplifiers to improve the performance of an NFT-based communication system. To overcome the ISI caused by the chromatic dispersion-induced signal broadening, we append the signal with cyclic extension in time domain, Fig. 10. Each signal, carrying one QAM symbol, is extended for the value greater than the channel memory calculated from the signal bandwidth Δv [53]:

$$\mu = 2\pi |\beta_2| \Delta v L, \quad (10)$$

where L is the link length. In our simulations, the symbols

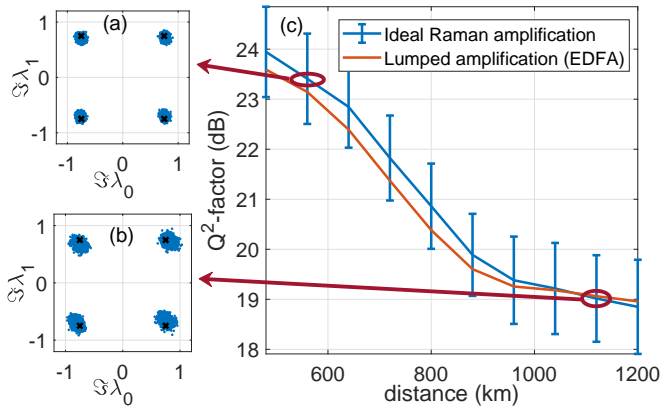


Fig. 9: a) The received constellation at 580 km, b) the received constellation at 1120 km, and c) Q^2 -factor for a 4-QAM 1 Gsym/s signal with -5 dBm power against distance. We used ideal Raman amplification (blue) and EDFA (red), $L_{span} = 80$ km, adding ASE noise.

are transmitted in “bursts” of $4M$ samples, where M is the size of the constellation. The burst is formed as follows: several signals, modulated using random data, are cyclically extended and put together. At the receiver, a simple phase rotation of the constellation is used to reduce the residual impact of ISI when the broadening is slightly larger than the

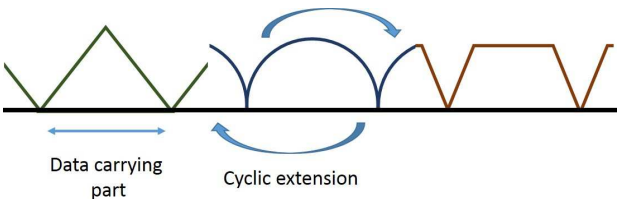


Fig. 10: Adding cyclic extension.

cyclic extension. Fig. 11c depicts the Q^2 -factor calculated from the EVM for four systems with different constellation sizes in a 880 km link. The Q^2 -factor is averaged over the number of symbols in each burst and over 2^8 runs. The symbol rate is 0.8 GSym/s; it can be increased by increasing the signal bandwidth (changing the real part of the eigenvalues). Fig. 11 shows that there is an optimum power at which the Q^2 -factor is maximal. One reason for a decline in the system performance at higher powers is the dependence of numerical accuracy on power, as is evident from Fig. 12b. Increasing the sampling rate and the accuracy of the arcs discretisation can improve the performance. Based on the Back-to-Back error shown in Fig. 12a, an over-sampling ratio of $N = 128$ is chosen considering the trade off between the effective noise, complexity and the numerical accuracy. The received constellations at optimum power are shown in Fig. 11 a, b, d, and e. As explained before, the axes of these scatter plots are the imaginary parts of the two eigenvalues in the discrete (main) spectrum of the received signal, $\Im \lambda_0$ and $\Im \lambda_1$, and points are centred to zero to facilitate comparison. Fig. 9c portrays the dependency of the Q^2 -factor on the link length and the impact of the particular amplification type: ideal Raman and EDFA. The close-to-ideal Raman amplification can be realised with a reasonable degree of accuracy through the second-order Raman pump [54]. In our simulations the signal power was set to -5 dBm, and the symbol rate is 1 Gsym/s. The received constellation is depicted at distances $z = 580$ km and $z = 1120$ km. We see that the system performances deteriorates quickly at long distances due to the ISI caused by the limited cyclic prefix duration. The performance can be improved by enlarging the duration of cyclic prefix.

Another important object in communication systems' design is the probability distribution function (PDF) of the received symbols. Finding the PDF of the received symbols given the transmitted ones is necessary to find the mutual information, channel capacity and to design an optimum coding and detection strategies. Since there is still a lack of a mathematical understanding of the behaviour of the PNFT spectrum quantities under the influence of optical noise [55], here we rely on the empirical PDF coming from the histogram of the received symbols. For a 1024-QAM signal, a 2D histogram of the received QAM symbols is plotted in Fig. 13 by using 2^9 symbols. The almost circular shapes in that figure indicate that the received distribution is close to the circular Gaussian one. However, as it is typically occurs in other communication systems based on the NFT [27], the characteristics of this Gaussian PDF differ for symbols with different signal power. This can be seen in Figs. 13b and c where the histogram of the small- and large-power parts of the constellation are shown. From this figure, an increase in the standard deviation is apparent for the symbols (constellation points) attributed to higher powers. These results are in agreement with the earlier ones reported in [55] for a PNFT system with different processing type. This observation suggests a Gaussian mixture model for the received points $\hat{\lambda}$, the PDF of which we can write

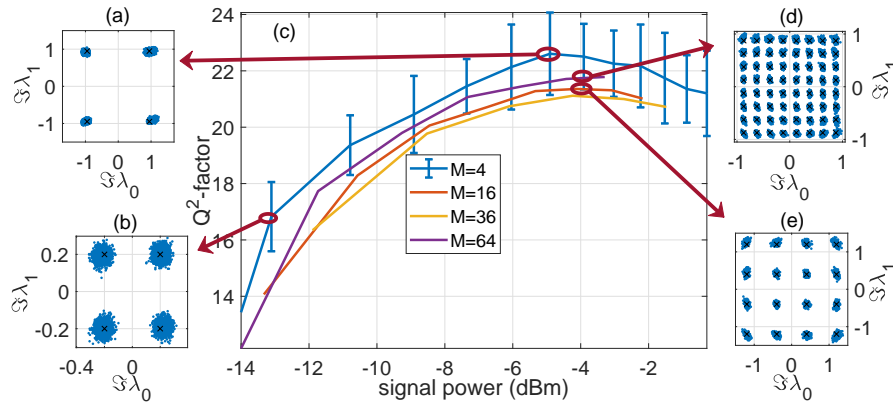


Fig. 11: a) The 4-QAM receiver constellation at the optimum power, b) the 4-QAM receiver constellation at power $P = -13.1$ dBm, c) Q^2 -factor for a 0.8 Gsym/s signal in a 880 km link with EDFA and ASE noise for various sizes of constellation, d) The 64-QAM, and e) the 16-QAM receiver constellation at the optimum power.

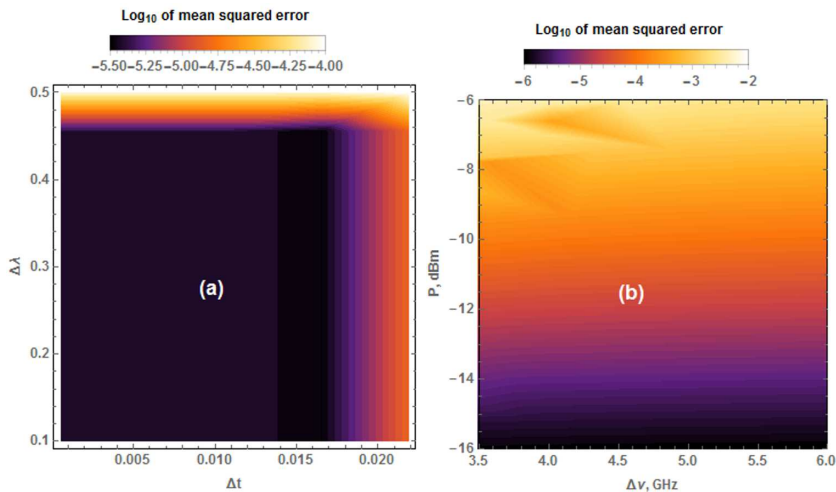


Fig. 12: Error of numerical computation of the points of the main spectrum from the NLSE solution, obtained from RHP solution a) against the resolution at the complex plane of parameter λ and temporal resolution Δt , and b) against the signal power P and bandwidth $\Delta\nu$.

down as

$$P(\hat{\lambda}) = \sum_{\lambda \in \Lambda} p_\lambda N(\hat{\lambda}; \lambda, \sigma_\lambda^2), \quad (11)$$

where Λ is the set of points in the constellation, p_λ is a probability function over Λ , and $N(\hat{\lambda}; \lambda, \sigma_\lambda^2)$ denotes a normal Gaussian distribution for the random variable $\hat{\lambda}$ with mean λ and variance σ_λ^2 . One of the most important metrics of a communication system performance is the mutual information of the transmitted and received symbols, here λ and $\hat{\lambda}$, respectively. Fig. 14 demonstrates the behaviour of the achievable mutual information as a functions of the link length. This figure, when compared with other discrete NFT spectrum communications systems such as eigenvalue and norming constants-based communications [59], indicates the good potential of the PNFT-based systems in rendering a high spectral efficiency.

VI. DISCUSSION AND CONCLUSION

In this work, we introduced a new approach utilising the RHP to the modulation, detection, and processing of

optical signal in NFT (or rather PNFT) based systems. We demonstrated how to construct a periodic signal with two arcs in its nonlinear spectrum by numerically solving a RHP, thus using the latter as a DSP tool in a fibre-optic communication system. Considering only two arcs (the simplest non-trivial case) simplifies the calculations and algorithms, however at the expense of our having a small number of the degrees of freedom per signal that can be simultaneously modulated. The lack of the direct precise control over the signal bandwidth and a relatively small spectral efficiency emerging due to the large time-bandwidth product are among the consequences of this choice. In a two-arc system, each signal carries just one QAM symbol. Therefore, the cyclic prefixes inserted to mitigate ISI and carrying no data produce a negative impact on the spectral efficiency value. However, we note that the important feature of our current approach is that it can be scaled up in a straightforward manner. So we can generally incorporate more arcs for our having more available parameters for the modulation, and then adjust

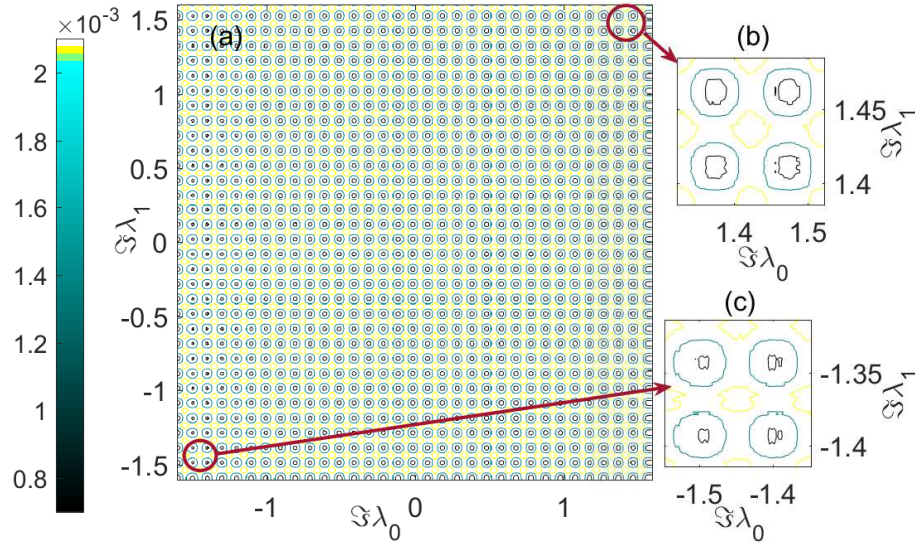


Fig. 13: a) A 2D histogram of the received constellation of a 1024-QAM system at distance $z = 680$ km and signal power $P = -5$ dBm, and a close up for two parts of the constellation attributed to b) the highest and c) the lowest signal power.

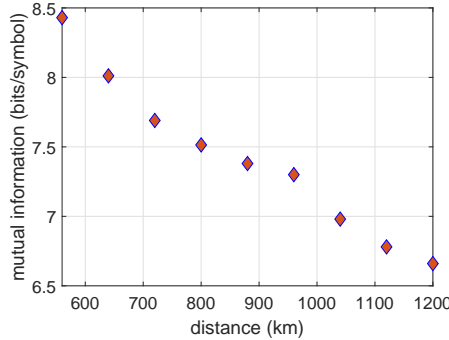


Fig. 14: The achievable mutual information versus the link length.

the system parameters to have a periodic solution. Then we can employ some parameters to set the bandwidth and power. In addition, we can potentially use the phases $\phi_{0,1}$, participating in the jump matrices definition (8), alongside with the main spectrum points, to convey more information. In this way, the ratio of the signal duration plus guard interval (cyclic prefix) to the number of bits encoded decreases, leading to a better spectral efficiency. However, this is left for future works, as at the moment we do not present any efficient receiver DSP design that could retrieve the phases. We also notice that a QAM constellation used in our current work may not be the best constellation or at least it can be improved by using probabilistic shaping, and the respective results will be reported in [60]. It is an interesting idea which we have been working on as a separate paper. At the end we note that solving the RHP requires extra caution in the case where the jump contour consists of open arcs, because its solution has, in general, singularities at the arc ends. The latter feature would inevitably affect the numerical implementation. Appendix C shows the way of how we

cope with this problem by transforming the original RHP to that with the contours consisting of closed arcs. In this work, the RHP solver `RHSolve` from [49] is used as a black box, and we notice that it was not optimally designed for our purpose, of course. The next step is to design such a flexible RHP solver package in which the desired problem-specific adjustments are possible and the accuracy is well controllable.

VII. ACKNOWLEDGEMENTS

This work was partially supported by the Leverhulme Project RPG-2018-063.

APPENDIX A NONLINEAR SPECTRUM OF A PERIODIC SOLUTION OF THE NLSE

Nonlinear spectrum of a periodic solution to the NLSE is obtained through the spectral analysis of the Zakharov-Shabat operator Eq. (2), where z is a parameter. Writing it in the form

$$\begin{bmatrix} \partial_t + i\lambda & -q(t, z) \\ q(t, z)^* & \partial_t - i\lambda \end{bmatrix} \Phi = 0 = \mathcal{L}\Phi, \quad (12)$$

the spectrum of this operator considered in $L^2(-\infty, \infty)$ is defined as the collection of those values of the spectral parameter λ , for which: 1) \mathcal{L} fails to be bijective, or 2) the inverse operator is not bounded. In terms of solutions of (12), for λ in the spectrum there exist a bounded non-trivial solution of (12). Determine these two independent solutions to Eq. (12) by imposing two initial values at a base point t_0 [39] and suppressing the dependence on z

$$\theta(t_0, t_0; \lambda) = \begin{bmatrix} 1 \\ 0 \end{bmatrix}, \quad \text{and} \quad \phi(t_0, t_0; \lambda) = \begin{bmatrix} 0 \\ 1 \end{bmatrix}. \quad (13)$$

The fundamental matrix made by these two solutions, being evaluated at one period T after the base point, is called the monodromy matrix:

$$\mathcal{M} = \begin{bmatrix} \theta_1(t_0, t_0 + T; \lambda) & \phi_1(t_0, t_0 + T; \lambda) \\ \theta_2(t_0, t_0 + T; \lambda) & \phi_2(t_0, t_0 + T; \lambda) \end{bmatrix}, \quad (14)$$

with $\det \mathcal{M} = 1$ and the trace $\Delta(\lambda) = \text{Tr} \mathcal{M}$, called the discriminant, independent of the base point. In the Floquet theory for the Zakharov-Shabat operator with periodic coefficients, its Bloch solution Ψ is determined as an eigenfunction of the operator of shift by the period:

$$\psi(t + T; \lambda) = m(\lambda)\psi(t; \lambda), \quad (15)$$

where $m(\lambda)$ is called the Floquet multiplier. Clearly, ψ is bounded on the whole line for those λ , for which $|m(\lambda)| = 1$. On the other hand, being a solution of the Zakharov-Shabat system, ψ is a combination of θ and ϕ at any time:

$$\begin{aligned} \psi(t_0 + T; \lambda) &= A\phi(t_0, t_0 + T; \lambda) + B\theta(t_0, t_0 + T; \lambda) \\ &= \mathcal{M} \begin{bmatrix} A \\ B \end{bmatrix}. \end{aligned}$$

Combining this with Eq. (15), it follows that

$$m(\lambda) \begin{bmatrix} A \\ B \end{bmatrix} = \mathcal{M} \begin{bmatrix} A \\ B \end{bmatrix}, \quad (16)$$

i.e., $m(\lambda)$ is an eigenvalue of the monodromy matrix \mathcal{M} . Since $\det \mathcal{M} = 1$, two eigenvalues, $m_+(\lambda)$ and $m_-(\lambda)$, are determined by $\Delta(\lambda)$:

$$m_{\pm}(\lambda) = \frac{\Delta(\lambda) \pm \sqrt{\Delta^2(\lambda) - 4}}{2}, \quad (17)$$

from which we can realise that $\Delta(\lambda) \in [-2, 2]$ for the solution to be bounded. It follows that the continuous spectrum of the Zakharov-Shabat operator, which is where $|m(\lambda)| = 1$, can be characterized by the inequality $\Delta^2(\lambda) \leq 4$. For the end points $\lambda = \lambda_j$, we have $\Delta(\lambda_j) = \pm 2$ and thus $m(\lambda_j) = 1$ or $m(\lambda_j) = -1$, which, in view of (15), corresponds to the periodic or anti-periodic solutions of (12). Thus the end points of the spectral arcs (the main spectrum) can be found as the eigenvalues of the periodic or anti-periodic problem for (12) posed on the period interval.

Let λ belong to the spectrum associated to two Bloch solutions, ψ^+ and ψ^- . To construct a periodic solution to the NLSE, one can define squared eigenfunctions using these Bloch solutions as follows [39]:

$$\begin{aligned} f(t, z; \lambda) &= -\frac{i}{2}(\psi_1^+ \psi_2^- + \psi_2^+ \psi_1^-), \\ g(t, z; \lambda) &= \psi_1^+ \psi_1^-, \\ h(t, z; \lambda) &= -\psi_2^+ \psi_2^-. \end{aligned}$$

Having a finite-gap solution implies that these squared eigenfunctions are finite-order polynomials in λ . Straightforward calculations yield:

$$\begin{aligned} f^2 - gh &= -\frac{1}{4}W(\psi^+ \psi^-)^2 = \prod_{j=0}^N (\lambda - \lambda_j)(\lambda - \lambda_j^*), \\ g(t, z; \lambda) &= iq(t, z) \times \prod_{j=1}^N (\lambda - \mu_j(t, z)), \end{aligned} \quad (18)$$

where $W(\cdot)$ is the Wronskian and $\mu_j(t, z)$ are called the auxiliary spectrum, which represent the evolution of signal as it propagates through the fibre. To find $\mu_j(t, z)$ at any z and t , one needs to solve a system of differential equations, see [39]. The auxiliary spectrum lies on a Riemann surface defined by the first line of Eq. (18).

APPENDIX B DETAILS OF RHP STATEMENT

The inverse stage in the NFT presented in section III is based on the following observation [48]: $\Phi(t, z, \lambda)$ can be constructed using the solution of a RHP with the standard normalization and with jumps across Γ still independent of λ on each Γ_j . Namely,

$$\Phi(t, z; \lambda) = e^{(if_0t + ig_0z)\sigma_3} \mathbf{M}(t, z; \lambda) e^{-(if(\lambda)t + ig(\lambda)z)\sigma_3}, \quad (19)$$

where:

- 1) $f(\lambda)$ and $g(\lambda)$ are scalar functions analytic in $\mathbb{C} \setminus \Gamma$ satisfying the following conditions: (i) $f(\lambda) = \lambda + f_0 + O(1/\lambda)$ and $g(\lambda) = 2\lambda^2 + g_0 + O(1/\lambda)$ as $\lambda \rightarrow \infty$, with some constants f_0 and g_0 ; (ii) the limiting values of f and g across Γ are related by

$$f_+(\lambda) + f_-(\lambda) = C_j^f, \quad g_+(\lambda) + g_-(\lambda) = C_j^g, \quad j = 0, \dots, N,$$

with some real constants C_j^f and C_j^g .

- 2) The matrix \mathbf{M} is the solution of the RHP with (i) the jump conditions $\mathbf{M}^-(t, z, \lambda) = \mathbf{M}^+(t, z, \lambda) \mathbf{G}_j(t, z)$, $\lambda \in \Gamma_j$, where

$$\mathbf{G}_j(t, z) = \begin{pmatrix} 0 & ie^{-i(C_j^f t + C_j^g z + \phi_j)} \\ ie^{i(C_j^f t + C_j^g z + \phi_j)} & 0 \end{pmatrix}, \quad (20)$$

and (ii) the normalization condition $\mathbf{M} \rightarrow I$ as $\lambda \rightarrow \infty$.

In turn, finding \mathbf{M} can be reduced to solving a linear integral equation. Indeed, if $\mu = \mu(t, z, \xi)$, $\xi \in \Sigma = \cup_j \Gamma_j$ is the solution of the integral equation (with respect to ξ ; t and z are parameters) $\mu - \mathcal{C}_G \mu = I$, where the operator \mathcal{C}_G is defined as follows:

$$(\mathcal{C}_G f)(t, z, \xi) := \frac{1}{2\pi i} \int_{\Sigma} \frac{f(s)(\mathbf{G}(t, z, s) - I)}{s - \xi^-} ds, \quad \xi \in \Sigma, \quad (21)$$

(in our case, $\mathbf{G}(t, z, s)$ is piecewise constant w.r.t. s : $\mathbf{G}(t, z, s) = \mathbf{G}_j(t, z)$ for $s \in \Gamma_j$). Then \mathbf{M} can be expressed in terms of μ as follows:

$$\mathbf{M}(t, z, \lambda) = I + \frac{1}{2\pi i} \int_{\Sigma} \frac{\mu(t, z, \xi)(\mathbf{G}(t, z, \xi) - I)}{\xi - \lambda} d\xi, \quad \lambda \in \mathbb{C} \setminus \Sigma.$$

In terms of \mathbf{M} , the expression for $q(t, z)$ takes the form

$$q(t, z) = 2i(\mathbf{M}_1)_{1,2}(t, z) e^{2if_0t + 2ig_0z}, \quad (22)$$

where $\mathbf{M}_1(t, z)$ is determined by the asymptotic relations $\mathbf{M}(t, z, \lambda) = I + \mathbf{M}_1/\lambda + O(\lambda^{-2})$ as $\lambda \rightarrow \infty$. Alternatively, q can be expressed in terms of μ by

$$q(t, z) = -\frac{1}{\pi} \int_{\Sigma} (\mu(t, z, \xi)(\mathbf{G}(t, z, \xi) - I))_{1,2} ds.$$

Notice that if one sets $C_0^f = C_0^g = 0$, then the conditions in 1) determine uniquely C_j^f and C_j^g for $j = 1, \dots, N$, as well

as the quantities f_0 and g_0 . Namely, if $\mathcal{N} \geq 3$, then C_j^f and C_j^g are respectively the unique solutions of the systems of linear algebraic equations

$$\begin{aligned} \sum_{j=1}^{\mathcal{N}} C_j^f \int_{\Gamma_j} \frac{\xi^k d\xi}{w(\xi)} &= 0, \quad k = 0, \dots, \mathcal{N}-2, \\ \sum_{j=1}^{\mathcal{N}} C_j^f \int_{\Gamma_j} \frac{\xi^{\mathcal{N}-1} d\xi}{w(\xi)} &= -2\pi i, \end{aligned} \quad (23)$$

and

$$\begin{aligned} \sum_{j=1}^{\mathcal{N}} C_j^g \int_{\Gamma_j} \frac{\xi^k d\xi}{w(\xi)} &= 0, \quad k = 0, \dots, \mathcal{N}-3, \\ \sum_{j=1}^{\mathcal{N}} C_j^g \int_{\Gamma_j} \frac{\xi^{\mathcal{N}-2} d\xi}{w(\xi)} &= -4\pi i, \\ \sum_{j=1}^{\mathcal{N}} C_j^g \int_{\Gamma_j} \frac{\xi^{\mathcal{N}-1} d\xi}{w(\xi)} &= -2\pi i \sum_{j=0}^{\mathcal{N}} (\lambda_j + \lambda_j^*). \end{aligned} \quad (24)$$

If $\mathcal{N} = 1$, then C_1^f and C_1^g are determined by the last equations in (23) and (24) (cf. (28)); if $\mathcal{N} = 2$, then C_j^f , $j = 1, 2$ are defined by the system in general form (23) whereas C_j^g , $j = 1, 2$ are determined by the system of two last equations in (24). Then $f(\lambda)$ is determined, for all $\mathcal{N} \geq 1$, by

$$f(\lambda) = \frac{w(\lambda)}{2\pi i} \sum_{j=1}^{\mathcal{N}} \int_{\Gamma_j} \frac{C_j^f d\xi}{w(\xi)(\xi - \lambda)}, \quad (25)$$

whereas $g(\lambda)$ is given by

$$g(\lambda) = \frac{w(\lambda)}{2\pi i} \sum_{j=1}^{\mathcal{N}} \int_{\Gamma_j} \frac{C_j^g d\xi}{w(\xi)(\xi - \lambda)}$$

for $\mathcal{N} \geq 2$ and by

$$g(\lambda) = 2w(\lambda) + \frac{w(\lambda)}{2\pi i} \int_{\Gamma_1} \frac{C_1^g d\xi}{w(\xi)(\xi - \lambda)}$$

for $\mathcal{N} = 1$. In turn, f_0 and g_0 are determined from the asymptotic relations: $f(\lambda) = \lambda + f_0 + O(1/\lambda)$ and $g(\lambda) = 2\lambda^2 + g_0 + O(1/\lambda)$ as $\lambda \rightarrow \infty$ ($f(\lambda)$ and $g(\lambda)$ are given by the expressions above).

The finite-genus solutions are quasi-periodic in t but not, in general, periodic. On the other hand, in order to arrive at periodic NLSE solutions, see (22), it is sufficient to require all the frequencies C_j^f , $j = 1, \dots, \mathcal{N}$ supplemented by f_0 to be commensurable. Indeed, if this is the case, then all the jump matrices $\mathbf{G}_j(t, z)$, see (20), have a common period, which implies (due to the uniqueness of the solution of the RHP) that the solution $\mathbf{M}(t, z, \lambda)$ of the RHP is periodic w.r.t. t , with the same period, for all z and λ ; consequently, $(\mathbf{M}_1)_{1,2}(t, z)$ in (22) is also periodic w.r.t. t with the same period. Notice that the periodicity is not affected by ϕ_j 's in (20), which can thus be arbitrarily chosen (as real parameters). On the other hand, the additional constraint

$$\sum_{j=1}^{\mathcal{N}} C_j^f \int_{\Gamma_j} \frac{\xi^{\mathcal{N}} d\xi}{w(\xi)} = -i\pi \sum_{j=0}^{\mathcal{N}} (\lambda_j + \lambda_j^*), \quad (26)$$

provides that $f_0 = 0$ in (22). In turn, the commensurability of C_j^f , $j = 1, \dots, \mathcal{N}$ can be ensured by an appropriate choice of λ_j . Indeed, the system (23) complemented by (26) can be viewed as a system of $\mathcal{N}+1$ complex equations: given C_j^f , $j = 1, \dots, \mathcal{N}$, determine $\mathcal{N}+1$ complex parameters $\{\lambda_j\}_{j=0}^{\mathcal{N}}$.

Now let us consider the simplest non-trivial case, i.e., the case $\mathcal{N} = 1$. In this case, the problem of ensuring periodicity is greatly simplified: it is sufficient to ensure that $f_0 = 0$, which, in turn, can be done by simultaneously shifting all the spectral data points $\{\lambda_j\}_{j=0}^{\mathcal{N}}$ along the real axis. Thus a preliminary step in the construction of a genus-1 solution consists in the adjustment of the main spectrum: given $\{\hat{\lambda}_j\}_{j=0}^1$, the real-valued shift is computed as follows:

$$\hat{f}_0 = \frac{\int_{\hat{\Gamma}_1} \frac{\xi d\xi}{\hat{w}(\xi)}}{\int_{\hat{\Gamma}_1} \frac{d\xi}{\hat{w}(\xi)}} - \frac{1}{2} \sum_{j=0}^1 (\hat{\lambda}_j + \hat{\lambda}_j^*) \quad (27)$$

with $\hat{w}(\xi) = \hat{w}_+(\xi)$, where $\hat{w}_+(\xi)$ is the limiting value from the (+) side of $\hat{\Gamma}_1$ (according to the orientation shown in Fig. 4) of the function $\hat{w}(\lambda) = \sqrt{\prod_{j=0}^1 (\lambda - \hat{\lambda}_j)(\lambda - \hat{\lambda}_j^*)}$ defined with the cuts $\hat{\Gamma}_{0,1}$ along the arcs $(\hat{\lambda}_{0,1}, \hat{\lambda}_{0,1}^*)$, where the branch is fixed by the condition $\hat{w}(\lambda) \sim \lambda^2$ as $\lambda \rightarrow \infty$. Then the new points λ_j , corresponding to a periodic genus-1 solution with $f_0 = 0$ (see (22)), are defined by: $\lambda_j = \hat{\lambda}_j + \hat{f}_0$. Now, given $\{\lambda_j\}_{j=0}^1$ and ϕ_1 (setting $\phi_0 = 0$), the procedure of construction of a genus-1 solution consists of the following steps.

(i) Calculate

$$C^f = -\frac{2\pi i}{\int_{\Gamma_1} \frac{d\xi}{w(\xi)}}, \quad C^g = C^f \sum_{j=0}^1 (\lambda_j + \lambda_j^*), \quad (28)$$

where $w(\xi)$ is defined as above, with $\hat{\lambda}_{0,1}$ replaced by $\lambda_{0,1}$.

(ii) Define the jump matrices:

$$\begin{aligned} \mathbf{G}_0 &= \begin{bmatrix} 0 & i \\ i & 0 \end{bmatrix}, \\ \mathbf{G}_1(t, z) &= \begin{bmatrix} 0 & -1/\theta(t, z) \\ \theta(t, z) & 0 \end{bmatrix}, \end{aligned} \quad (29)$$

where $\theta(t, z) = ie^{i(C^f t + C^g z + \phi_1)}$ and $C^{f,g}$ are defined by (28).

(iii) Solve the matrix RHP: given \mathbf{G}_j , $j = 0, 1$, find a 2×2 -valued function $\mathbf{M}(\cdot, \cdot, \lambda)$ analytic in $\mathbb{C} \setminus \{\Gamma_0 \cup \Gamma_1\}$ and satisfying the following conditions:

$$\begin{aligned} \mathbf{M}^-(t, z, \lambda) &= \mathbf{M}^+(t, z, \lambda) \mathbf{G}_j(t, z), \quad \text{for } \lambda \in \Gamma_j, \quad j = 0, 1, \\ \mathbf{M}(t, z, \lambda \rightarrow \infty) &\rightarrow \mathbf{I}. \end{aligned} \quad (30)$$

(iv) Calculate $\mathbf{M}_1(t, z)$ from the asymptotic expansion:

$$\mathbf{M}(t, z, \lambda) = \mathbf{I} + \mathbf{M}_1(t, z) \lambda^{-1} + O(\lambda^{-2}) \text{ as } \lambda \rightarrow \infty.$$

(v) Retrieve the solution of the NLSE by

$$q(t, z) = 2i(\mathbf{M}_1)_{1,2}(t, z).$$

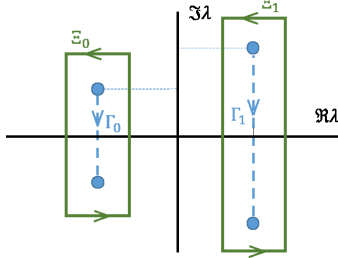


Fig. 15: Closed contours $\Xi_{0,1}$, enveloping the arcs $\Gamma_{0,1}$ for alternative RHP to avoid singularity points.

APPENDIX C

RHP CONTOUR DEFORMATION TO AVOID SINGULARITIES AT THE ENDS OF OPEN ARCS

Solving RHP with jumps on open arcs (or, equivalently with discontinuous jumps on closed contours) faces the problem of singularities at the arc ends, which affects numerical solutions of the associated integral equations. To remedy this, the original RHP can be transformed to a problem with (continuous) jumps on closed contours.

Introduce two (rectangular in our simulations) contours $\Xi_{0,1}$ enveloping the arcs $\Gamma_{0,1}$ with reasonable offset (see Fig. 15), define the functions

$$\kappa_j(\lambda) = \left(\frac{\lambda - \lambda_j}{\lambda - \lambda_j^*} \right)^{1/4} \quad (31)$$

for $\lambda \in \mathbb{C} \setminus \Gamma_j$ (the branch is fixed by the condition $\kappa_j(\lambda) \rightarrow 1$ as $\lambda \rightarrow \infty$), and define the matrices $\mathbf{K}_{0,1}$ by

$$\mathbf{K}_0(\lambda) = \frac{1}{2} \begin{pmatrix} \kappa_0(\lambda) + \frac{1}{\kappa_0(\lambda)} & -\kappa_0(\lambda) + \frac{1}{\kappa_0(\lambda)} \\ -\kappa_0(\lambda) + \frac{1}{\kappa_0(\lambda)} & \kappa_0(\lambda) + \frac{1}{\kappa_0(\lambda)} \end{pmatrix}$$

and

$$\mathbf{K}_1(t, z, \lambda) = \frac{1}{2} \begin{pmatrix} \kappa_1(\lambda) + \frac{1}{\kappa_1(\lambda)} & \frac{\kappa_1(\lambda) - \frac{1}{\kappa_1(\lambda)}}{i\theta(t, z)} \\ i\theta(t, z) \left(\kappa_1(\lambda) - \frac{1}{\kappa_1(\lambda)} \right) & \kappa_1(\lambda) + \frac{1}{\kappa_1(\lambda)} \end{pmatrix}.$$

Introduce $\hat{\mathbf{M}}$ by

$$\hat{\mathbf{M}} = \begin{cases} \mathbf{M}\mathbf{K}_j^{-1}, & \text{inside } \Xi_j, \\ \mathbf{M}, & \text{outside } \Xi_j, \end{cases}$$

where \mathbf{M} is the solution of the original RHP (30). Then $\hat{\mathbf{M}}$ satisfies the RHP with jump continuous on each closed part Ξ_j of the total contour:

$$\begin{aligned} \hat{\mathbf{M}}^-(t, z, \lambda) &= \hat{\mathbf{M}}^+(t, z, \lambda)\mathbf{K}_j, \quad \lambda \in \Xi_j, \quad j = 0, 1, \\ \hat{\mathbf{M}}(t, z, \lambda \rightarrow \infty) &\rightarrow \mathbf{I} \end{aligned} \quad (32)$$

(notice that $\hat{\mathbf{M}}$, in contrast to \mathbf{M} , has no jumps across $\Gamma_{0,1}$). Such a problem can be efficiently solved numerically using the RHP solver [49]. On the other hand, the solution $\hat{\mathbf{M}}$ of the RHP (32) still gives rise to the genus-1 solution of the NLSE by $q(t, z) = 2i(\hat{\mathbf{M}}_1)_{1,2}(t, z)$.

Presented RHP deformation makes the numerical computation more reliable for further communication applications.

APPENDIX D EVALUATION OF THE NUMERICAL ACCURACY OF THE PROPOSED METHOD

In order to understand the impact of the numerical errors on the overall performance of a communication system, the back-to-back error is calculated. Given a pair of complex points with their imaginary parts as the degrees of freedom, a signal is constructed solving the RHP. The points of the main spectrum of this signal is then calculated (see Appendix A), and the average of the displacement in the imaginary parts of these points is considered as the error. Two numerical procedures contribute to this error: inverse transformation (Riemann-Hilbert solver) and direct transformation (Ablowitz-Ladik algorithm). The first error is directly controllable by the resolution at the complex plane of parameter λ (designated below as $\Delta\lambda$, related to the number of spectral points, n) The location of the points of the main spectrum determines the signal power (through the imaginary part) and signal bandwidth (through the real part). However, due to our particular method of constructing a periodic signal with the predetermined period, the real part of these points depend slightly on the imaginary part. Since the data is carried by the imaginary parts of these points, this slight change in the real parts is irrelevant as long as we are able to separate two spectral arcs at the receiver.

On the other hand, the accuracy of the direct transform is known to depend on the resolution in the temporal domain, Δt , signal power and bandwidth. Fig. 12a depicts the dependency of the numerical error (mean of imaginary parts squared differences) on $\Delta\lambda$ and Δt (keeping the bandwidth value around 5 GHz, like in our transmission system simulations). As it is evident from this figure, error falls as resolutions increase until the point beyond which the impact is insignificant. The improvement through decreasing Δt also plateaus at a very large number of samples. The effect of the signal power and bandwidth on the accuracy is illustrated in Fig. 12b, which shows an almost constant trend against bandwidth but a sharp decline as the signal power grows, which, as in the following, shows itself in the overall performance of the system (see Fig. 11). For fair comparison we kept the temporal discretisation Δt in the range 1-2 ps, what is significantly lower than the inverse signal bandwidth. Hereafter, we fix the discretisation of the arcs, n , and Δt considering its impact on the effect of amplifier noise, which linearly grows with bandwidth.

REFERENCES

- [1] A. Hasegawa and T. Nyu, "Eigenvalue communication," *J. Lightwave Technol.* **11**, pp. 395–399 (1993)
- [2] V. E. Zakharov and A. B. Shabat, "Exact theory of two-dimensional self-focusing and one-dimensional selfmodulation of waves in nonlinear media," *Soviet Physics-JETP* **34**, pp. 62–69 (1972).
- [3] M. I. Yousefi and F. R. Kschischang, "Information Transmission Using the Nonlinear Fourier Transform, Parts I – III," *IEEE Trans. Inf. Theory* **60**, pp. 4312–4369 (2014).

- [4] S. K. Turitsyn, J. E. Prilepsky, S. T. Le, S. Wahls, L. L. Frumin, M. Kamalian, and S. A. Derevyanko, "Nonlinear Fourier transform for optical data processing and transmission: advances and perspectives," *Optica* **4**, 3, pp. 307–322 (2017).
- [5] M. I. Yousefi and X. Yangzhang, "Linear and Nonlinear Frequency-Division Multiplexing," in 42nd European Conference and Exhibition on Optical Communications (ECOC), pp. 342–344 (2016).
- [6] S. T. Le, J. E. Prilepsky, and S. K. Turitsyn, "Nonlinear inverse synthesis for high spectral efficiency transmission in optical fibers," *Opt. Express* **22**, 22, pp. 26720–26741 (2014).
- [7] S. T. Le, V. Aref, and H. Buelow, "Nonlinear signal multiplexing for communication beyond the Kerr nonlinearity limit," *Nat. Photon.* **11**, 9, p. 570 (2017).
- [8] S. T. Le, and H. Buelow, "64 × 0.5 Gbaud Nonlinear Frequency Division Multiplexed Transmissions With High Order Modulation Formats," *J. Lightwave Technol.* **35**, 17, pp. 3692–3698 (2017).
- [9] S. T. Le, I. D. Phillips, J. E. Prilepsky, P. Harper, A. D. Ellis, and S. K. Turitsyn, "Demonstration of nonlinear inverse synthesis transmission over transoceanic distances," *J. Lightwave Technol.* **34**, 10, pp. 2459–2466 (2016).
- [10] S. T. Le, I. D. Phillips, J. E. Prilepsky, M. Kamalian, A. D. Ellis, P. Harper, and S. K. Turitsyn, "Achievable Information Rate of Nonlinear Inverse Synthesis Based 16QAM OFDM Transmission," in 42nd European Conference and Exhibition on Optical Communications (ECOC), pp. 1–3 (2016).
- [11] X. Yangzhang, D. Lavery, P. Bayvel, and M. I. Yousefi, "Impact of Perturbations on Nonlinear Frequency-Division Multiplexing," *J. Lightwave Technol.* **36**, 2, pp. 485–494 (2018).
- [12] J.-W. Goossens, H. Hafermann, M. I. Yousefi, and Y. Jaouën, "Nonlinear Fourier Transform in Optical Communications," in Conference on Lasers and Electro-Optics Europe & European Quantum Electronics Conference (CLEO/Europe-EQEC), paper CI_1_3 (2017).
- [13] M. J. Ablowitz and H. Segur, *Solitons and the Inverse Scattering Transform* (SIAM, 1981).
- [14] R.-J. Essiambre, G. Kramer, P. J. Winzer, G. J. Foschini, and B. Goebel, "Capacity limits of optical fiber networks," *J. Lightwave Technol.* **28**, 4, pp. 662–701 (2010).
- [15] P. P. Mitra and J. B. Stark, "Nonlinear limits to the information capacity of optical fiber communications," *Nature* **411**, 6842, pp. 1027–1030 (2001).
- [16] S. Civelli, E. Forestieri, and M. Secondini, "Impact of discretization and boundary conditions in nonlinear frequency-division multiplexing," Photonic Technologies (Fotonica 2016), 18th Italian National Conference on, pp. 1-4 (2016).
- [17] S. Civelli, E. Forestieri, and M. Secondini, "Why Noise and Dispersion may Seriously Hamper Nonlinear Frequency-Division Multiplexing," *IEEE Photon. Tech. Lett.* **29**, 16, pp. 1332–1335 (2017).
- [18] T. Gui, C. Lu, A. P. T. Lau, and P. K. A. Wai, "High-order modulation on a single discrete eigenvalue for optical communications based on nonlinear Fourier transform," *Opt. Express* **25**, 17, pp. 20286–20297 (2017).
- [19] S. Gaiarin, A. M. Perego, E. P. da Silva, F. Da Ros, and D. Zibar, "Dual-polarization nonlinear Fourier transform-based optical communication system," *Optica* **5**, 3, pp. 263–270 (2018).
- [20] S. T. Le, V. Aref and H. Buelow, "High Speed Precompensated Nonlinear Frequency-Division Multiplexed Transmissions," *J. Lightwave Technol.* **36**, 6, pp. 1296–1303 (2018).
- [21] I. Lima, V. Grigoryan, M. O'Sullivan, and C. Menyuk, "Computational complexity of nonlinear transforms applied to optical communications systems with normal dispersion fibers," *Proc. IEEE Photonics Conference*, Reston, pp. 277–278 (2015).
- [22] I. T. Lima, T. D. S. DeMenezes, V. S. Grigoryan, M. O'Sullivan, and C. R. Menyuk, "Nonlinear Compensation in Optical Communications Systems With Normal Dispersion Fibers Using the Nonlinear Fourier Transform," *J. Lightwave Technol.* **35**, 23, pp. 5056–5068 (2017).
- [23] J. E. Prilepsky, S. A. Derevyanko, K. J. Blow, I. Gabitov, and S. K. Turitsyn, "Nonlinear Inverse Synthesis and Eigenvalue Division Multiplexing in Optical Fiber Channels," *Phys. Rev. Lett.* **113**, art. no. 013901 (2014).
- [24] M. Kamalian, J. E. Prilepsky, S. T. Le, and S. K. Turitsyn, "Periodic nonlinear Fourier transform for fiber-optic communications, Part I: theory and numerical methods," *Opt. Express* **24**, pp. 18353–18369 (2016).
- [25] J. C. Cartledge, F. P. Guiomar, F. R. Kschischang, G. Liga, and M. P. Yankov, "Digital signal processing for fiber nonlinearities," *Opt. Express* **25**, 3, pp. 1916–1936 (2017).
- [26] M. Kamalian, J. E. Prilepsky, S. T. Le, and S. K. Turitsyn, "Periodic nonlinear Fourier transform for fiber-optic communications, Part II: eigenvalue communication," *Opt. Express* **24**, pp. 18370–18381 (2016).
- [27] S. A. Derevyanko, J. E. Prilepsky, and S. K. Turitsyn, "Capacity estimates for optical transmission based on the nonlinear Fourier transform," *Nat. Commun.* **7**, art. no. 12710 (2016).
- [28] M. Kamalian, J. E. Prilepsky, S. T. Le, and S. K. Turitsyn, "Spectral efficiency estimation in periodic nonlinear Fourier transform based communication systems," in Optical Fiber Communication Conference (OFC), paper Th2A-54 (2017).
- [29] A. R. Its, and V. B. Matveev, "The periodic Korteweg-deVries equation," *Funct. Anal. Appl.* **9**, 67 (1975).
- [30] A. I. Bobenko, and L. A. Bordag "Periodic multiphase solutions of the Kadomsev-Petviashvili equation," *J. of Physics A: Mathematical and General*, **22**, 9, p. 1259–1274 (1989).
- [31] I. M. Krichever, "The spectral theory of two-dimensional periodic operators and applications," *Russ. Math. Surv.* **44**, pp. 121–184 (1989).
- [32] Y. Ma, and M. J. Ablowitz, "The periodic cubic Schrödinger equation," *Stud. Appl. Math.* **65**, pp. 113–

- 158 (1981).
- [33] H. C. Yuen, and B. M. Lake, "Nonlinear dynamics of deep-water gravity waves," *Adv. Appl. Mech.* **22**, pp. 67–229 (1982).
- [34] N. Akhmediev, A. Ankiewicz, and M. Taki, "Waves that appear from nowhere and disappear without a trace," *Phys. Lett. A* **373**, pp. 675–678 (2009).
- [35] A. R. Osborne, *Nonlinear Ocean Waves and the Inverse Scattering Transform*, Academic Press (2010).
- [36] A. Calini, and C. M. Schober, "Characterizing JONSWAP rogue waves and their statistics via inverse spectral data," *Wave Motion* **71**, p. 5–17 (2017).
- [37] O. R. Its and V. P. Kotlyarov, "Explicit formulas for the solutions of a nonlinear Schrödinger equation," *Doklady Akad. Nauk Ukrainian SSR, ser. A*, vol. 10, 965–968 (1976); English translation available on-line at <http://arxiv.org/abs/1401.4445v1>.
- [38] V. B. Matveev, "30 years of finite-gap integration theory," *Philosophical Transactions of the Royal Society of London A: Mathematical, Physical and Engineering Sciences* **366**, pp. 837–875 (2008).
- [39] E. R. Tracy and H. H. Chen, "Nonlinear self-modulation: an exactly solvable model," *Phys. Rev. A* **37**, pp. 815–839 (1988).
- [40] E. D. Belokolos, A. I. Bobenko, V. Z. Enolski, A. R. Its, V. B. Matveev, *Algebro-geometric Approach in the Theory of Integrable Equations*, Springer Series in Nonlinear Dynamics, Springer, Berlin, 1994.
- [41] S. Wahls, and H. V. Poor, "Fast numerical nonlinear Fourier transforms," *IEEE Trans. Inf. Theory*, **61**, 6957–6974 (2015).
- [42] A. O. Smirnov, "Periodic two-phase "rogue waves"," *Math. Notes* **94**, pp. 897–907 (2013).
- [43] M. Kamalian Kopae, J. E. Prilepsky, S. T. Le, and S. K. Turitsyn, "Optical communication based on the periodic nonlinear Fourier transform signal processing," *IEEE 6th International Conference on Photonics (ICP)*, Kuching, Malaysia, pp. 1–3 (2016).
- [44] M. Kamalian Kopae, J. E. Prilepsky, S. T. Le, and S. K. Turitsyn, "Periodic nonlinear Fourier transform based optical communication systems in a band-limited regime," in Advanced Photonics (IPR, NOMA, Sensors, Networks, SPPCom, SOF). OSA Technical Digest, Vancouver, Canada, paper JTu4A.34, 2016.
- [45] M. Kamalian, J. E. Prilepsky, S. T. Le, and S. K. Turitsyn, "On the Design of NFT-Based Communication Systems With Lumped Amplification," *J. Lightwave Technol.* **35**, 24, pp. 5464–5472 (2017).
- [46] B. Deconinck, M. Heil, A. Bobenko, M. van Hoeij and M. Schmies, "Computing Riemann Theta Functions," *Math. Comp.* **73**, pp. 1417–1442 (2004).
- [47] T. Trogdon and S. Olver, *Riemann-Hilbert Problems, Their Numerical Solution, and the Computation of Nonlinear Special Functions*, SIAM (2016).
- [48] V. Kotlyarov and D. Shepelsky, "Planar unimodular Baker-Akhiezer function for the nonlinear Schrödinger equation," *Ann. Math. Sci. Appl.* **2**, pp. 343–384 (2017).
- [49] S. Olver, RHPackage for MATHEMATICA,
<http://www.maths.usyd.edu.au/u/olver/projects/RHPackage.html>
- [50] S. Olver, "A general framework for solving Riemann-Hilbert problems numerically," *Numerische Mathematik* **122**, pp. 305–340 (2012).
- [51] A. Kamchatnov, "New approach to periodic solutions of integrable equations and nonlinear theory of modulational instability," *Phys. reports* **286**, pp. 199–270 (1997).
- [52] M. Kamalian, A. Vasylchenkova, J. Prilepsky, D. Shepelsky, S. Turitsyn, "Communication System Based on Periodic Nonlinear Fourier Transform with Exact Inverse Transformation," To be presented at ECOC, Rome, Sweden, Sep. 2018.
- [53] E. Agrell, A. Alvarado, G. Durisi, and M. Karlsson, "Capacity of a Nonlinear Optical Channel With Finite Memory," *IEEE J. Lightwave Technol.* **32**, 16, pp. 2862–2876 (2014).
- [54] J. D. Ania-Castañón et al "Ultralong Raman fibre lasers as virtually lossless optical media," *Phys. Rev. Lett.* **96**, 2, 023902 (2006).
- [55] M. Kamalian, J. E. Prilepsky, S. T. Le, and S. K. Turitsyn, "Statistical Analysis of a Communication System Based on the Periodic Nonlinear Fourier Transform," Australian Conference on Optical Fibre Technology, Sydney, paper AT1C. 4 (2016).
- [56] S. Wahls, "Generation of Time-Limited Signals in the Nonlinear Fourier Domain via b-Modulation," in European Conference on Optical Communication (ECOC), Gothenburg, Sweden, Sep. 2017.
- [57] S. T. Le, K. Schuh, F. Buchali, and H. Buelow, "100 Gbps b-modulated Nonlinear Frequency Division Multiplexed Transmission," in Optical Fiber Communication Conference (OFC), paper W1G.6 (2018).
- [58] S. Wahls and V. Vaibhav, "Fast Inverse Nonlinear Fourier Transforms for Continuous Spectra of Zakharov-Shabat Type," arXiv preprint arXiv:1607.01305v2 (Dec. 2016).
- [59] H. Bülow, V. Aref and L. Schmalen, "Modulation on Discrete Nonlinear Spectrum: Perturbation Sensitivity and Achievable Rates," *IEEE Photonic Tech. Lett.*, Vol. **30**, p. 423–426 (2018).
- [60] M. Kamalian, A. Vasylchenkova, J. Prilepsky, D. Shepelsky, and S. Turitsyn, "Communication System Based on Periodic Nonlinear Fourier Transform with Exact Inverse Transformation," accepted in 44th European Conference and Exhibition on Optical Communications (ECOC), Sep. 2018.